2D WS_2 Liquid Crystals: Tunable Functionality Enabling Diverse Applications

Benjamin T. Hogan, Evgeniya Kovalska, Maria O. Zhukova, Murat Yildirim, Alexander Baranov, Monica F. Craciun and Anna Baldycheva.

Since the first synthesis of graphene in 2004[1,2], there has been a markedly rapid increase in the investigation of a wide range of atomically thin (two-dimensional – 2D) materials. In addition to graphene (exfoliated from graphite), materials that can be reduced to monolayer size have been shown to include: graphene oxide (from graphite oxide); transition metal dichalcogenides (TMDs)- for example molybdenum disulfide, tungsten disulfide, tungsten diselenide; and hexagonal boron nitride amongst countless others. The possibility of liquid crystalline states in dispersions of 2D materials owes to their intrinsic shape anisotropy. It has long been known (from theory described by Onsager in the 1940s) that both rigid and flexible anisotropic molecules or particles undergo an isotropic/liquid-crystalline transition as their concentration is raised[3], forming a lyotropic liquid crystal (LC). The main condition for this phase to be observed is that a significant anisotropy of the mesogens must exist; i.e. a large aspect ratio. This transition was initially observed with clay particles and variations on Onsager theory used to determine the phase diagram[4,5]. The transition concentration scales inversely with the aspect ratio (comparing the two large dimensions to the particle thickness); hence the requirement for a high aspect ratio, as the required concentration should be balanced against the solubility of the particles in the solvent used. As is observed in rigid rods[6,7] , the polydispersity of the dispersed molecules broadens the biphasic region in which both an isotropic phase and nematic phase can be observed. Hence it is desirable to have a low polydispersity of the dispersed particles. Additionally, pure solvents are wanted as the maximum isotropic concentration of the platelets and the ability to form liquid crystals is strongly influenced by impurities in the host solvent[8]. Recently, a new paradigm of significant interest for the development of novel functional materials where dynamic reconfigurability is delivered through the exploitation of liquid crystalline properties and 2D materials has emerged. Two-dimensional materials dispersed in specific host solvents have been shown to display lyotropic liquid crystalline phases within certain ranges of 2D material concentration[9–13], opening new routes within a wide variety of potential applications[14] from the deposition of highly uniform layers and heterostructures[11,15–22], to novel display device technologies[23–27]. The nanocomposites can be readily integrated on silicon chip by means of microfluidic technology allowing for dynamic control of the dispersed particles through the application of various on-chip stimuli[10].

To synthesise a LC based on 2D materials, one must first exfoliate the bulk material before dispersing in a solvent. There have been several methods developed by which 2D materials can be exfoliated,

each with their own advantages and disadvantages. Firstly, a mechanical cleavage method can be used (the so-called 'sticky-tape' method) where layers are separated by adhering one layer to a sticky surface and mechanically peeling it away from the bulk[1]. This method produces very pure materials with few defects induced and can also give relatively large areas of material coverage. However, this method has poor scalability and production of large quantities of 2D material is extremely time intensive. Alternatively, a vapour deposition method can be used where a 2D material is grown directly on a substrate from vapourised precursor molecules at very high temperatures[28–31]. This method can produce large areas of 2D material and can be scaled to produce large quantities. However, there are numerous sources for the introduction of defects in the material including substrate induced defects and impurities in the vapours used amongst others, the material must be transferred from the substrate after deposition which can be problematic, and the production cost and time are prohibitive to adoption at larger scales. However, adoption of these materials in novel device applications, and in synthesising liquid crystalline dispersions, is often limited by challenges surrounding the scalability, cost of production processes or limited quality of materials produced.

To overcome the limitations in scalability, liquid phase exfoliation has been developed as a method where a bulk material is dispersed in a solvent and then layers are broken apart[15,32–34]. In most cases, the layers are broken apart using ultrasonication where high frequency sound waves are transmitted through the dispersion[15,32–38]. The sound waves induce the formation of bubbles and cavities between layers which break the layers apart as they expand. However, they also cause strains in the material which cause intralayer cleavage of the particles, reducing the size of the particles obtained after exfoliation. The use of intercalating surfactants to weaken the interlayer forces before exfoliation can greatly increase the yield of the exfoliation[15,33], but the subsequent removal of the surfactant is liable to damage the quality of the exfoliated product. Other than ultrasonication, other methods have been developed for liquid phase exfoliation, including strong acid induced oxidation reactions causing cleavage[39] and freezing of water intercalated layered structures where expansion of water as it freezes causes interlayer cleavage[40]. Following exfoliation, particles of specific sizes can be isolated by centrifugation of the dispersion[41,42], solvent induced selective sedimentation[43] or by pH-assisted selective sedimentation[44] amongst others. Liquid phase exfoliation techniques are inherently scalable and therefore highly promising for adoption in device fabrication processes as 2D material liquid crystals make the breakthrough to widespread use.

Supplementary Methods

Development of liquid crystalline samples:

Starting from bulk WS_2 particles (Sigma-Aldrich 243639), with dimensions around five microns on average (maximum particle dimensions were observed to be on the order of 10-15 µm), dispersions were produced in a range of solvents (water, isopropanol, chloroform, tetrahydrofuran, methanol, acetone and ethanol), with a range of concentrations (0.01-5 $mg.mL^{-1}$). To accurately compare the effect of different solvents, it was necessary to have homogeneous particle size distributions between samples. Hence, an initial 500 *mL* dispersion was prepared, with IPA as the solvent, at a concentration of 5 $mg.mL^{-1}$, in a sealed beaker.

To break down the material a process of ultrasonication in an ultrasonic bath (James Products 120W High Power 2790ml Ultrasonic Cleaner) filled with deionised water was used. Five, hour-long, periods, separated by 30 minutes each to prevent excessive heating of the solvent, were used to

ensure sufficient exfoliation of the sample. The resultant dispersions were then put through a process of centrifugation for 10 minutes at 2000 *rpm* to remove residual bulk material and narrow the distribution of particle sizes present in the dispersion.

After centrifugation, the dispersion was fractioned, with only the supernatant extracted, to ensure only suitably sized particles remained. The resultant dispersion was then dried under vacuum (~0.1 *atm*) in a Schlenk line to fully remove the solvent, before being re-dispersed in the required solvents for the final dispersions.

Redispersion involved transfer of a suitable mass of the exfoliated tungsten disulfide to give the desired concentration into small volumes (<5 *mL*) of IPA, chloroform and THF. After re-dispersion, the dispersions were again ultrasonicated (for a few minutes) to prevent any aggregated exfoliated particles remaining in the dispersions. As the concentration is changed significantly following the centrifugation step, it is necessary to re-establish the concentration following that step. The re-dispersion process allowed for accurate knowledge of the concentrations of the dispersions. Additionally, as all steps up until redispersion were the same for all samples, the size distribution of particles in the dispersion is as uniform as possible between samples. It is known from the extensive literature[45–47] on liquid phase exfoliation of 2D materials that both the solvent and concentration can have significant effects on the yield and size distribution obtained. Hence, the process used here offers the significant advantage of allowing direct comparability between dispersions, to the greatest degree achievable.

Samples dispersed in other solvents (e.g. water, ethanol etc.) were produced by the same methods, but using a different initial dispersion. Hence, direct comparability cannot be claimed. However, these samples did not display any indications of liquid crystallinity.

Development of unexfoliated samples:

The unused fraction from the synthesis of the LC samples was used to produce the unexfoliated samples. This fraction was dried and redispersed using the same process as described for the exfoliated fraction that gave the better liquid crystallinity.

Development of non-LC samples:

Non-LC samples were produced to compare the films producible using the LC state to those given without it. The same tungsten disulfide powder was dispersed at a concentration of 5 $mg.mL^{-1}$ in IPA. This dispersion was then ultrasonicated for 2 minutes to ensure dispersion with minimal exfoliation. No optical anisotropy was observable in the dispersions.

Supplementary Results

Analysis of WS_2 particle sizes was undertaken by five separate methods:

1) Optical microscopy
2) Raman spectroscopy
3) Dynamic light scattering (DLS)
4) Scanning electron microscopy (SEM)
5) Atomic force microscopy (AFM)

Using optical microscopy, it was determined that ‘unexfoliated’ particles had typical sizes of 1-10µm, with the mean size around 5µm x 5µm and that exfoliated particles had typical dimensions of around

500nm up to a few microns in length and width with mean size around 2µm x 2µm. This characterisation also revealed the presence of occasional much larger particles with bulk like characteristics. From Raman spectroscopy, the thickness of unexfoliated particles was determined to be predominantly bulk-like from Raman spectroscopy, although determination of any shape anisotropy was not possible with Raman spectroscopy for which accurate determination of thickness is limited beyond ~10 layers. For exfoliated particles, typical thicknesses of 1-10 layers were observed.

Dynamic light scattering (DLS) measurements were performed to analyse the particle sizes in the dispersion, in addition to microscopy and Raman spectroscopy of individual drop-cast flakes. Sizes found from dynamic light scattering were in agreement with those obtained by the other methods. For example, for the dispersion in chloroform, broad peaks were observed at four different particle sizes: 3.98 *nm*; 93.9 *nm*; 320 *nm*; 1610 *nm*. The first peak is indicative of flakes on the order of few-layer thickness being present in the dispersion. The last peak is in agreement with the average flake lateral sizes being on the order of a micron. However, this technique cannot quantitatively analyse the numbers of particles possessing each size measured, so simply serves as a qualitative assessment of the ranges of particle sizes present. We note from the literature[48] that DLS has been used previously to accurately establish the lateral particle sizes in solution and has been verified against other characterisation methods. The accurate determination thickness however has never been reported. However, we suggest that it should be possible to accurately obtain both the thickness and lateral sizes of the particles, provided that the orientation of the particles can be fixed. Typically particles dispersed in a liquid will have random orientations and move and change orientation randomly due to Brownian motion. However, the key property of lyotropic liquid crystalline phases is that the orientation of the dispersed particles is not random, but generally aligned along a director. Domains will then exist with the dispersion with different directors. Of course, the different directors for different domains mean that when considering a large volume of the dispersion, there is no overall average director, but rather the orientation of the particles is still effectively random. However, it is also well-known that interfaces between liquid crystals and other materials can cause preferential alignment of the director due to anchoring of the mesogens at the surface; this being a key concept in their use in liquid crystal displays. In our case, if the tungsten disulfide particles in the LC state align at the interface with the cuvette used for DLS measurements, with a director either parallel or perpendicular to the interface, then the scattering cross-section for those particles is

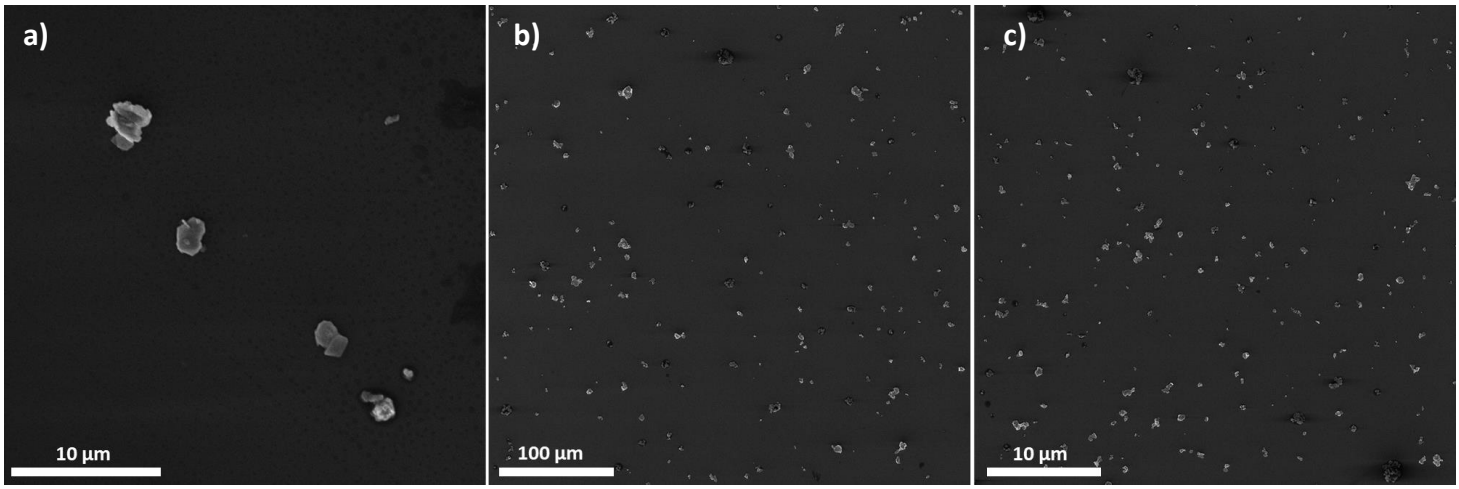

Supplementary Figure 1: a) SEM image of a few drop cast WS_2 particles, representative of the mix of aggregation, defects and more pristine particles observed throughout the drop cast particles**. b,c)** SEM images of multiple WS_2 particles drop cast on silicon-on-insulator.

fixed, non-random, and suitably aligned relative to the incoming light. Hence it would be possible to obtain the thickness and lateral sizes of the particles. We suggest that this alignment occurs during our measurements, allowing the accurate determination of the sizes that we observe, as verified by other methods.

SEM was also used. Particles were drop-cast onto a silicon-on-insulator substrate and then imaged (Supplementary Fig. 1). From the images produced, the size of the particles present was analysed, with over 400 individual particles measured. A range of particle sizes from 508 *nm* up to 11.06 *µm* was observed. The mean lateral particle size was determined to be 2.61 *µm*, while the mode of the particle size distribution was determined as 1.63 *µm* and the median value was 2.34 *µm*. This is in close agreement with the 1610 *nm* peak seen in the DLS spectrum, particularly when considering that the peak value reported in the DLS spectrum would correspond to the modal value. It was also noticed that there were some significantly smaller particles (<500 *nm*), which are likely responsible for the DLS peaks at 93.9 *nm* and 320 *nm*. These particles were excluded from the size analysis.

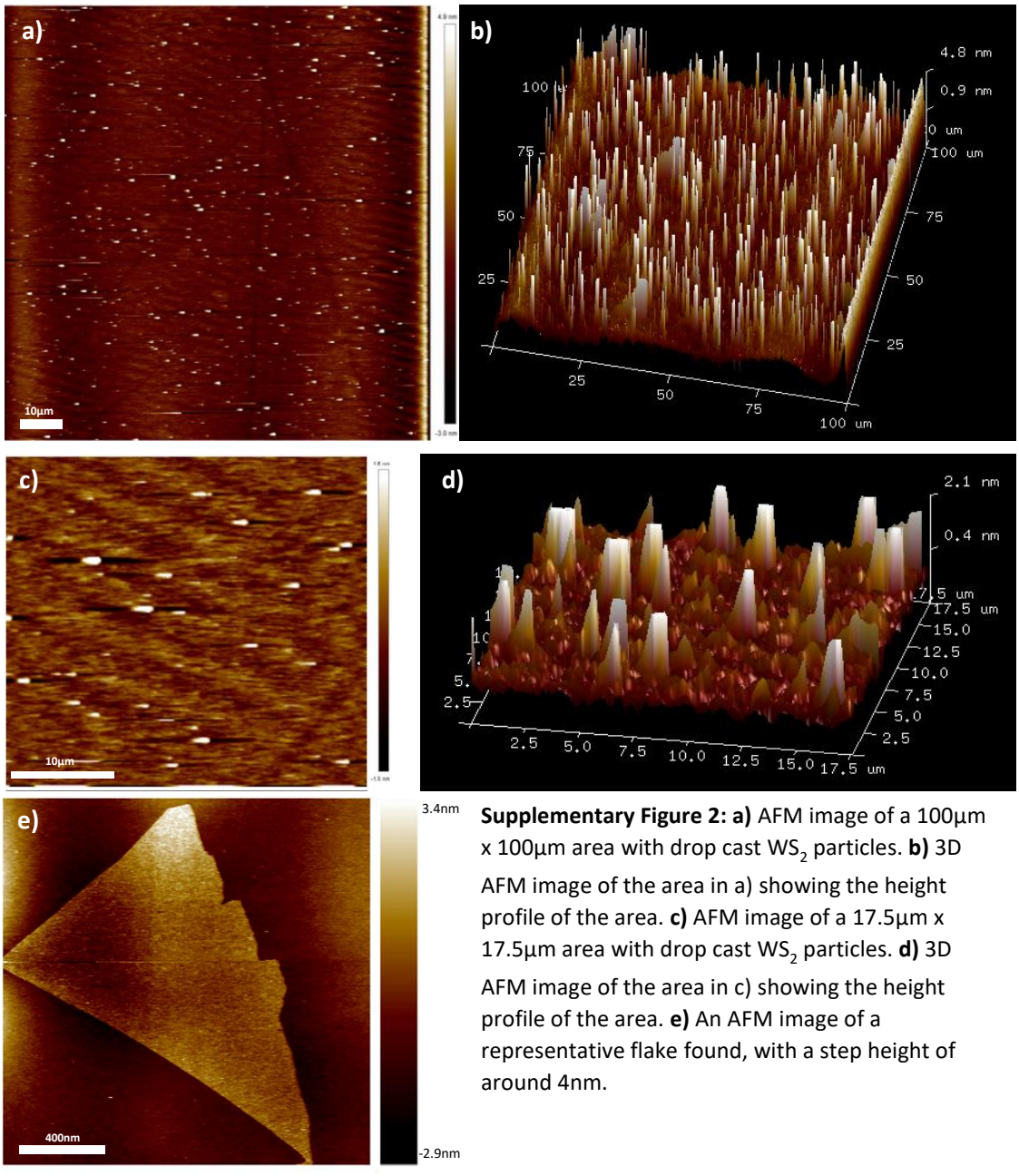

Supplementary Figure 2: a) AFM image of a 100µm x 100µm area with drop cast WS_2 particles. **b)** 3D AFM image of the area in a) showing the height profile of the area. **c)** AFM image of a 17.5µm x 17.5µm area with drop cast WS_2 particles. **d)** 3D AFM image of the area in c) showing the height profile of the area. **e)** An AFM image of a representative flake found, with a step height of around 4nm.

AFM images were also produced for the drop-cast particles (Supplementary Fig. 2). The step heights for each of these particles was measured. From analysis of the step heights for a large number of particles, an average thickness of around 4 *nm* was observed, again in close agreement with the peak in the DLS spectrum attributed to the particle thickness. For example, in the area shown in Supplementary Fig. 2c-d, a subset of 20 particles were found. The step heights of these particles were: 5.830; 1.186; 2.875; 1.985; 4.030; 5.337; 2.744; 2.709; 1.893; 4.034; 2.354; 2.467; 4.611; 6.331; 4.961; 3.094; 4.721; 7.902; 6.34 and 4.161 *nm* respectively – giving an average height of 3.978 *nm* (corresponding to approximately 6.5 layers). A more thorough analysis of a greater number of particles (578) over a large area gave a similar figure, with an average thickness of 4.04 *nm* (6.63 layers). Histograms showing the distributions of particle sizes (with statistical averages marked also) are presented in Supplementary Figure 3.

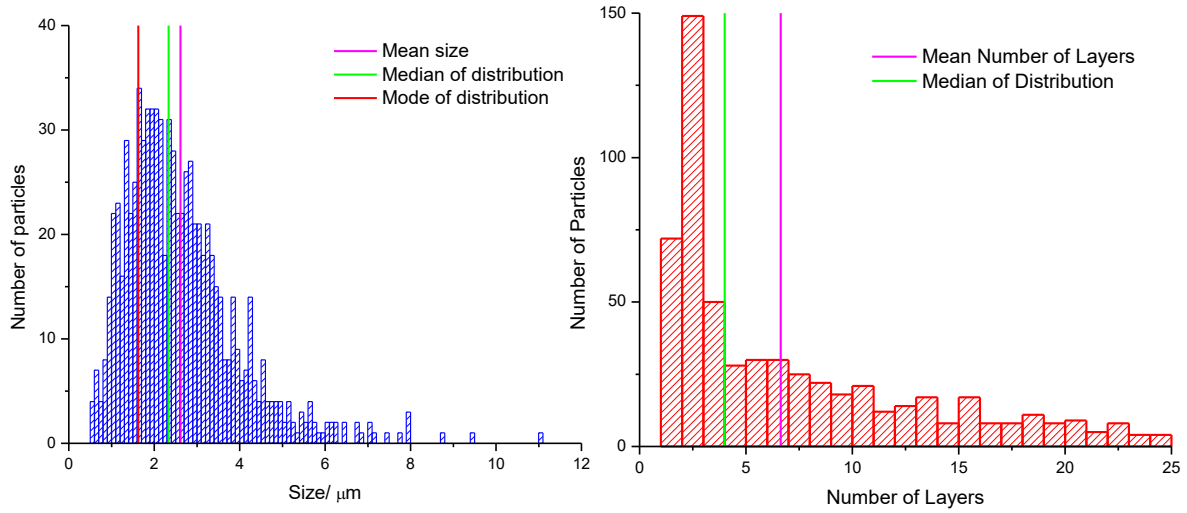

Supplementary Figure 3: Histograms of the measured distributions of: **a)** lateral sizes of WS_2 particles as determined from SEM, with the arithmetic mean (purple), median (green) and mode(red) of the distribution shown; **b)** thickness of WS_2 particles as determined from AFM, with the arithmetic mean (purple) and median (green) of the distribution shown.

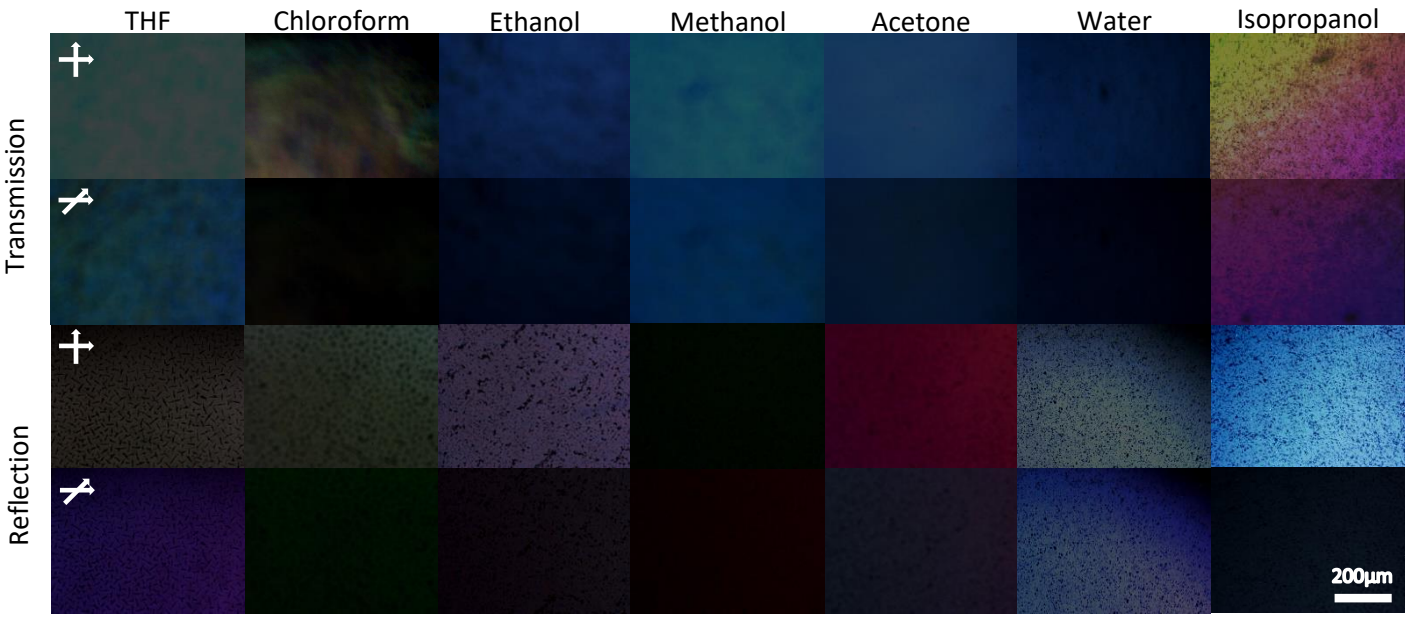

Supplementary Figure 4: Optical microscopy images of the reflection and transmission from tungsten disulfide dispersions in different solvents, with crossed polarisers at 90° and 45°.

Under illumination by linearly polarised light, microscopy images taken through an analyser with polarisation at 90 and 45 to that of the incident light are shown in Supplementary Figure 4. Some texturing is observed when looking at the reflection from the liquid surfaces for a range of solvents. However, there are many challenges to imaging these liquids optically. When looking at reflection from the liquids, self-assembly or aggregation at the substrate interfaces is observed. Self-assembly is particularly prevalent for chloroform- and tetrahydrofuran-based dispersions. It is known that the liquid crystallinity of dispersions of anisotropic rigid board-like particles can be suppressed by confined geometries such as those existing near interfaces[13]. When looking at the transmission, there is some texturing observable. However, to prevent the aggregation seen for small confined volumes, a greater volume of the dispersion was required. With a sufficient volume, there is a high level of absorption to be overcome. To overcome this further barrier, an intense light source was required, along with longer exposure times for the images. As the dispersions are produced in organic solvents with low viscosity, there is significant Brownian motion. Hence, for longer image exposure times, there is blurring of the images due to this Brownian motion. Additionally, greater intensity of the light source can allow significant transmission of light through the crossed polarisers regardless of any change in polarisation as the light passes through the material, due to the imperfection of the polarisers' absorbance. As such, we can observe bright states for dispersions in solvents such as ethanol, methanol, acetone and water despite there being no evidence of liquid crystallinity for those dispersions. However, it is not necessary to

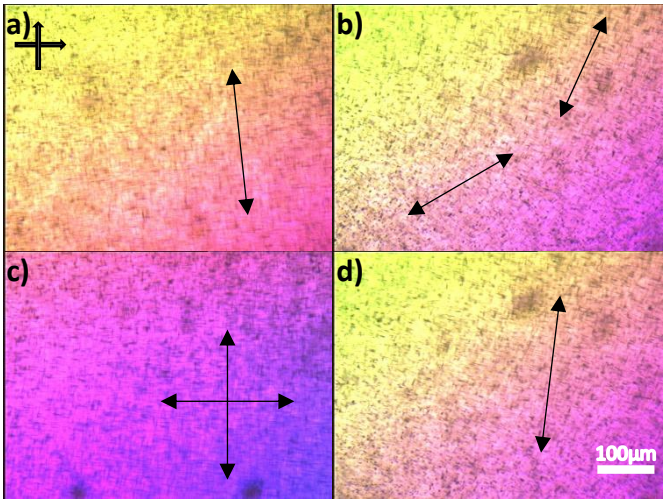

Supplementary Figure 5: a-d) Polarised optical microscopy images of a dispersion of WS_2 in IPA at a concentration of 0.5 $mg.mL^{-1}$. The polariser and analyser were oriented orthogonally. The arrows indicate the observed directions of particle alignment in the images.

use crossed polarisers to observe the textures of these liquid crystals. Figure 2 in the main text shows the bright and dark states that exist in the liquid crystal dependent on the flake orientation relative to the incident light. These bright and dark states are clearly visible without the need for polarising optics[26]. Supplementary figure 5 shows polarised optical microscopy images of a WS2 dispersion in IPA. In these images, by looking closely, we can observe the general directional ordering of the dispersed particles directly (shown as black arrows o the images).

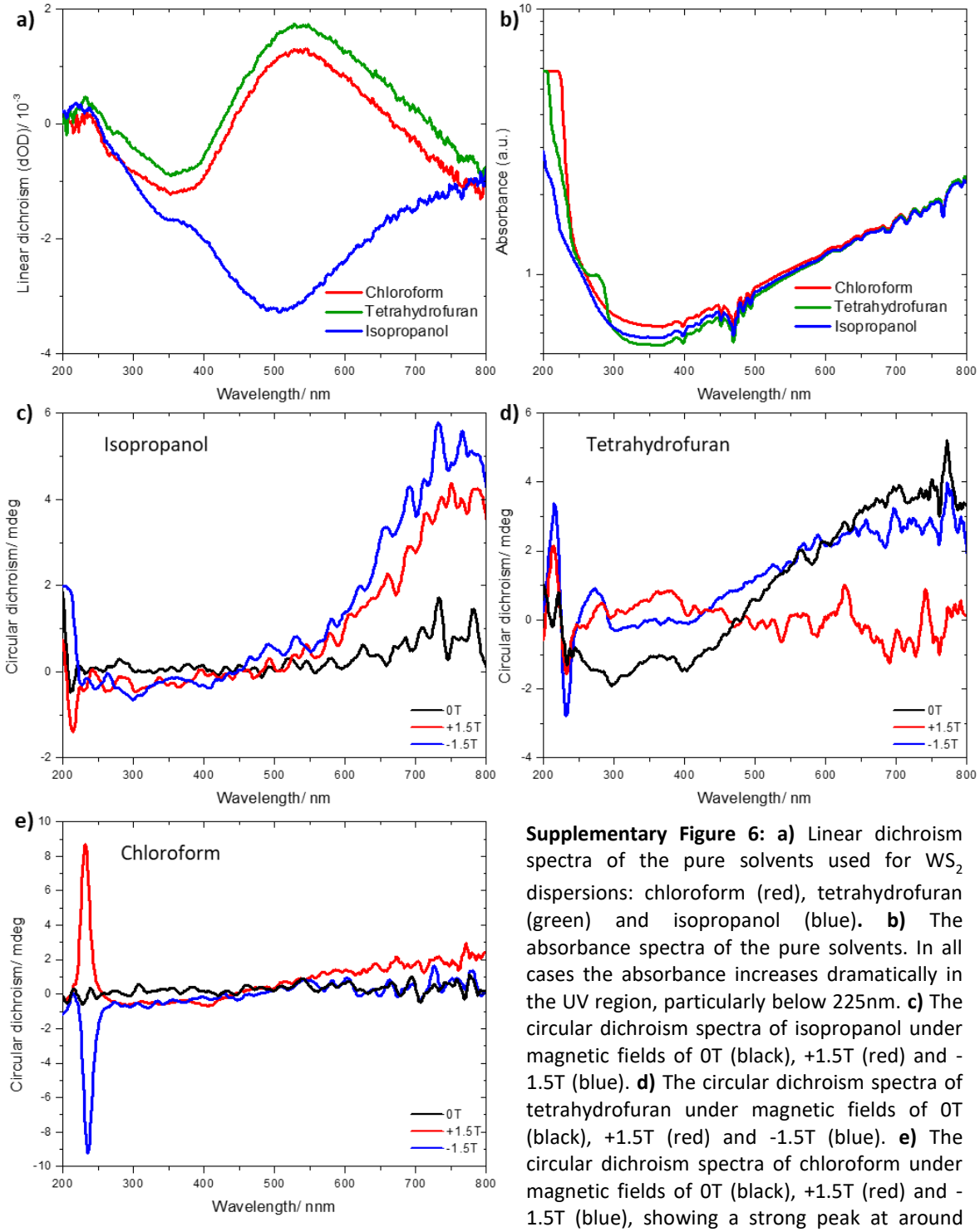

Supplementary Figure 6: a) Linear dichroism spectra of the pure solvents used for WS_2 dispersions: chloroform (red), tetrahydrofuran (green) and isopropanol (blue)**. b)** The absorbance spectra of the pure solvents. In all cases the absorbance increases dramatically in the UV region, particularly below 225nm. **c)** The circular dichroism spectra of isopropanol under magnetic fields of 0T (black), +1.5T (red) and -1.5T (blue). **d)** The circular dichroism spectra of tetrahydrofuran under magnetic fields of 0T (black), +1.5T (red) and -1.5T (blue). **e)** The circular dichroism spectra of chloroform under magnetic fields of 0T (black), +1.5T (red) and -1.5T (blue), showing a strong peak at around 230nm under applied magnetic field.

The linear and circular dichroism, along with the absorption spectra of the solvents (in the cuvettes used) are presented for reference (Supplementary Fig. 6). The linear dichroism of dispersions at different concentrations was measured, in addition to that for isopropanol shown in the main text. Similar trends are observable, with the degree of birefringence increasing with concentration (Supplementary Fig. 7).

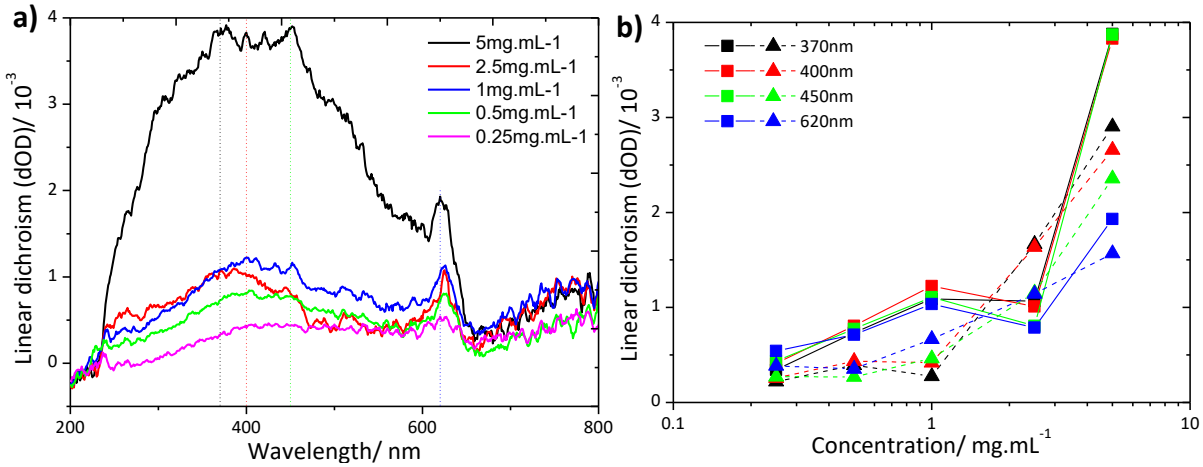

Supplementary Figure 7: a) Linear dichroism of dispersions of tungsten disulfide in chloroform at different concentrations. **b)** Linear dichroism of dispersions of tungsten disulfide in chloroform at specific wavelengths; solid lines (and squares) are for samples that had been exfoliated as described whereas dashed lines (and triangles) are for dispersions of much larger (unexfoliated) particles.

Deposition of thin films produced from filtering of the liquid crystalline dispersion was achieved in accordance with the method described by Shin *et al*[49]. Thin films produced in this manner were successfully transferred to: silicon for Raman mapping; Kapton for terahertz measurements. The general steps of the method followed were:

1) Rapid filtering from the LC crystal state to remove the solvent. For this purpose, polytetrafluoroethylene (PTFE) filter substrates were used with pore sizes of 0.02µm.
2) Transfer to the desired substrate through an IPA and heat-assisted lift-off process, as described in the literature. This process is compatible with many different substrates, including the silicon-on-insulator and Kapton substrates used in this work.

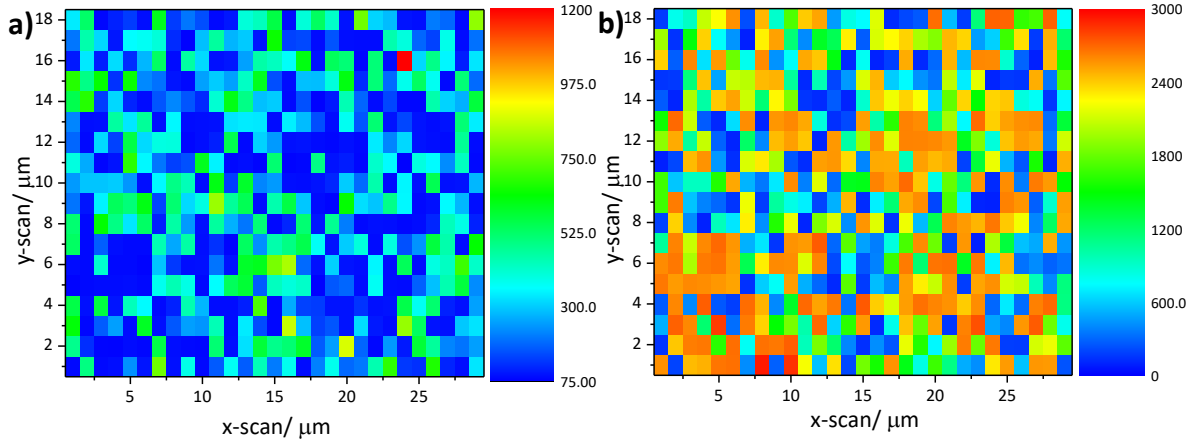

Supplementary Figure 8: a) Raman map of the A_{1g} peak of tungsten disulfide showing coverage across the whole surface for an area of 29µm x 18µm. **b)** Raman map of the silicon substrate peak, showing non-uniformity owing to the different thicknesses of tungsten disulfide coverage.

Raman maps were produced to show the coverage over large areas on silicon, deposited from the liquid crystalline dispersions. Coverage across a wide area is seen by looking at the A_{1g} peak of tungsten disulfide (Supplementary Fig. 8a), which is found to always be present in the spectra. The coverage is non-uniform in terms of layer thicknesses of the individual flakes as well as the overall film thickness, hence the variable intensity. The film thickness (and possibly density) inhomogeneity is also evident from the variable intensity of the silicon substrate peak in the Raman spectra (Supplementary Fig. 8b). The optical image corresponding to the mapped area of the film is shown in Supplementary Figure 9. The approximate points at which individual Raman spectra were taken are shown by the green grid on the image, although there is some misalignment between the internal optics used for imaging mapped areas, and the optics used for Raman scanning.

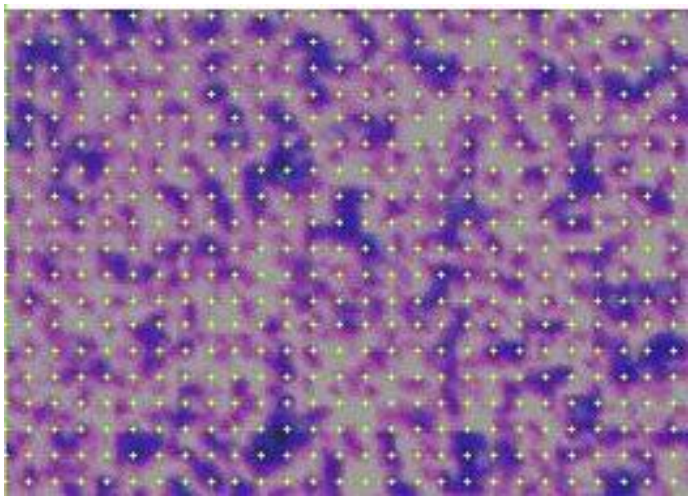

Supplementary Figure 9: Image of the area used for Raman mapping of the thin film transferred on silicon-on-insulator. Green dots represent the approximate positions at which the individual Raman spectra were taken. The grid spacing is 1µm in both the *x*- and *y*-directions.

We studied the transmission of samples in a broadband THz range (0.1–0.8 THz) by use of a laboratory terahertz time-domain spectrometer[50]. The experimental set-up scheme is presented in Supplementary Figure 10.

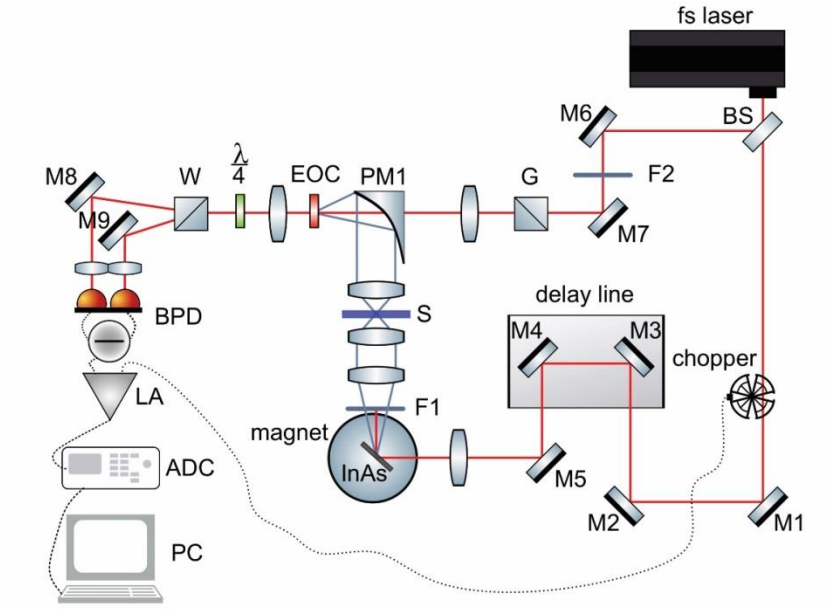

Supplementary Figure 10: THz time-domain spectrometer scheme. M1-9 – mirrors; BS – beam splitter; F1-F2 - IR filters; S – sample; PM1 – parabolic mirror; EOC – electro-optical crystal; W - Wollaston prism; BPD – balanced photodetector; LA – lock-in amplifier; ADC – analog-digital converter; PC – personal computer.

A femtosecond laser (fs laser - the active medium – Yb:KYW; λ = 1055 nm, pulse duration 100 fs, repetition rate 70 MHz, output power 3.8 W) radiation was divided by beam splitter (BS) into pump and probe beams. The pump beam was modulated by optical copper (OC), passed through a delay line

and focused into a THz generator (based on the photo-Dember effect and electron shifting) that consists of a bulk InAs semiconductor placed in a strong magnet field of 2.4 T. Generated radiation passed through a polytetrafluoroethylene filter (F1) to cut off the pump beam, followed by lenses and the sample (S), with some absorption and refraction. To detect THz generation, an electro-optic method was used ([100]) CdTe crystal (EOC)). The polarization of the probe beam was fixed by a Glan prism (G) to 45° relative to the THz radiation polarization. The induced change in polarization was measured by a system consisting of a quarter-wave plate (λ/4), Wollaston prism (W), mirrors M_8, M_9, and a balanced photodetector (BPD). An amplified signal was transmitted to a computer (PC) via an analog-to-digital converter (ADC).

The parameters of THz radiation were: spectral range from 0.01 to 1.5 THz with maximum at 0.595 THz, average power 30 μW, FWHM 0.45 ps.

We obtained the time dependence of the electric field $E_{ref}(t)$ of the THz pulse (Supplementary Fig. 11), so we can then calculate the complex reference spectrum of the THz pulse $G_{ref}(\omega)$, by calculating the Fourier transform of the corresponding time sequence. By placing the required object in the path of THz radiation, it is possible to measure the change in the temporal form of the THz pulse and the complex spectrum of radiation transmitted through it – $E_{obj}(\omega)$ and $G_{obj}(\omega)$.

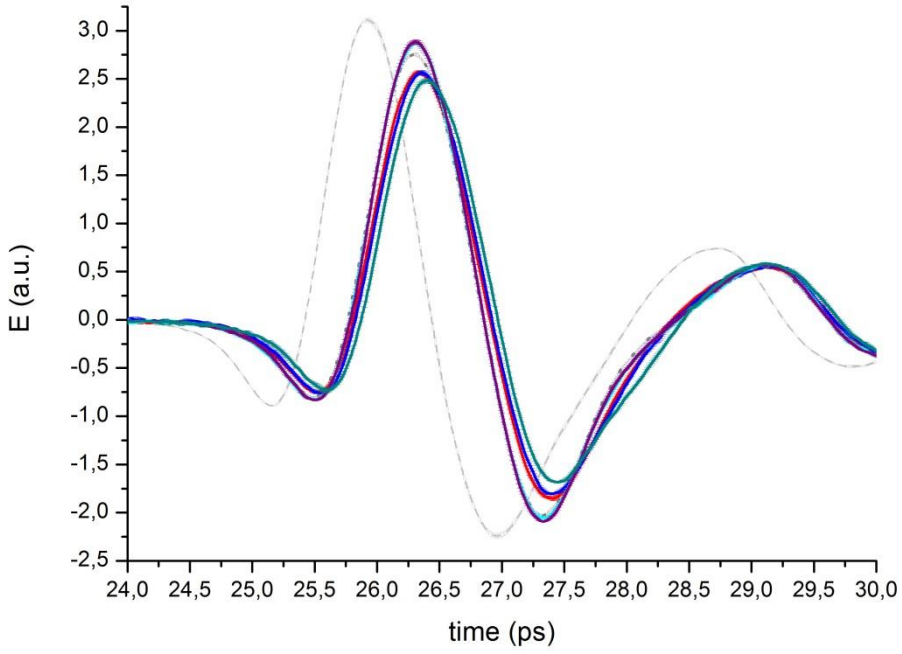

Supplementary Figure 11. Time dependences of the electric field *E*(t) of the terahertz pulses through: air reference (grey dashed), Kapton substrate (blue dashed) and WS_2 on Kapton (solid lines).

The transmission spectra of samples were calculated using the following relationship:

$$T_{layer+Kapton}(\omega) = \frac{\left|G_{layer+Kapton}(\omega)\right|}{\left|G_{air}(\omega)\right|}$$

Supplementary references:

1 K. S. Novoselov, A. K. Geim, S. V Morozov, D. Jiang, Y. Zhang, S. V Dubonos, I. V Grigorieva and A. A. Firsov, *Science (80-.).*, 2004, **306**, 666–669.

2 A. C. Ferrari, F. Bonaccorso, V. Fal'ko, K. S. Novoselov, S. Roche, P. Bøggild, S. Borini, F. H. L. Koppens, V. Palermo, N. Pugno, J. A. Garrido, R. Sordan, A. Bianco, L. Ballerini, M. Prato, E. Lidorikis, J. Kivioja, C. Marinelli, T. Ryhänen, A. Morpurgo, J. N. Coleman, V. Nicolosi, L. Colombo, A. Fert, M. Garcia-Hernandez, A. Bachtold, G. F. Schneider, F. Guinea, C. Dekker, M. Barbone, Z. Sun, C. Galiotis, A. N. Grigorenko, G. Konstantatos, A. Kis, M. Katsnelson, L. Vandersypen, A. Loiseau, V. Morandi, D. Neumaier, E. Treossi, V. Pellegrini, M. Polini, A. Tredicucci, G. M. Williams, B. Hee Hong, J.-H. Ahn, J. Min Kim, H. Zirath, B. J. van Wees, H. van der Zant, L. Occhipinti, A. Di Matteo, I. A. Kinloch, T. Seyller, E. Quesnel, X. Feng, K. Teo, N. Rupesinghe, P. Hakonen, S. R. T. Neil, Q. Tannock, T. Löfwander and J. Kinaret, *Nanoscale*, 2015, **7**, 4598–4810.

3 L. Onsager, *Ann. N. Y. Acad. Sci.*, 1949, **51**, 627–659.

4 H. N. W. Lekkerkerker, F. M. van der Kooij and K. Kassapidou, *Nature*, 2000, **406**, 868–871.

5 M. A. Bates and D. Frenkel, *J. Chem. Phys.*, 1999, **110**, 6553.

6 M. J. Green, A. N. G. Parra-Vasquez, N. Behabtu and M. Pasquali, *J. Chem. Phys.*, 2009, **131**, 084901.

7 H. H. Wensink and G. J. Vroege, *J. Chem. Phys.*, 2003, **119**, 6868–6882.

8 D. van der Beek and H. N. W. Lekkerkerker, *Langmuir*, 2004, **20**, 8582–8586.

9 S. Li, M. Fu, H. Sun, Y. Zhao, Y. Liu, D. He and Y. Wang, *J. Phys. Chem. C*, 2014, **118**, 18015–18020.

10 B. T. Hogan, S. A. Dyakov, L. J. Brennan, S. Younesy, T. S. Perova, Y. K. Gun'ko, M. F. Craciun and A. Baldycheva, *Sci. Rep.*, 2017, **7**, 42120.

11 Z. Xu and C. Gao, *Nat. Commun.*, 2011, **2**, 571.

12 C. Zakri, C. Blanc, E. Grelet, C. Zamora-Ledezma, N. Puech, E. Anglaret and P. Poulin, *Philos. Trans. A. Math. Phys. Eng. Sci.*, 2013, **371**, 20120499.

13 I. Dierking and S. Al-Zangana, *Nanomaterials*, 2017, **7**, 305.

14 B. T. Hogan, E. Kovalska, M. F. Craciun and A. Baldycheva, *J. Mater. Chem. C*, 2017, **5**, 11185–11195.

15 N. Behabtu, J. R. Lomeda, M. J. Green, A. L. Higginbotham, A. Sinitskii, D. V Kosynkin, D. Tsentalovich, A. N. G. Parra-Vasquez, J. Schmidt, E. Kesselman, Y. Cohen, Y. Talmon, J. M. Tour and M. Pasquali, *Nat. Nanotechnol.*, 2010, **5**, 406–11.

16 R. Jalili, S. H. Aboutalebi, D. Esrafilzadeh, K. Konstantinov, S. E. Moulton, J. M. Razal and G. G. Wallace, *ACS Nano*, 2013, **7**, 3981–3990.

17 R. Jalili, S. Aminorroaya-Yamini, T. M. Benedetti, S. H. Aboutalebi, Y. Chao, G. G. Wallace and D. L. Officer, *Nanoscale*, 2016, **8**, 16862–16867.

18 M. Supur, K. Ohkubo and S. Fukuzumi, *Chem. Commun.*, 2014, **50**, 13359–13361.

19 M. G. Nasab and M. Kalaee, *RSC Adv.*, 2016, **6**, 45357–45368.

20 R. Jalili, S. H. Aboutalebi, D. Esrafilzadeh, R. L. Shepherd, J. Chen, S. Aminorroaya-Yamini, K. Konstantinov, A. I. Minett, J. M. Razal and G. G. Wallace, *Adv. Funct. Mater.*, 2013, **23**, 5345–5354.

21 A. Akbari, P. Sheath, S. T. Martin, D. B. Shinde, M. Shaibani, P. C. Banerjee, R. Tkacz, D.

Bhattacharyya and M. Majumder, *Nat. Commun.*, 2016, **7**, 10891.

22 K. Fu, Y. Wang, C. Yan, Y. Yao, Y. Chen, J. Dai, S. Lacey, Y. Wang, J. Wan, T. Li, Z. Wang, Y. Xu and L. Hu, *Adv. Mater.*, 2016, **28**, 2587–2594.

23 T.-Z. Shen, S.-H. Hong and J.-K. Song, *Nat. Mater.*, 2014, **13**, 394–9.

24 J. Y. Kim and S. O. Kim, *Nat. Mater.*, 2014, **13**, 325–326.

25 R. T. M. Ahmad, S.-H. Hong, T.-Z. Shen and J.-K. Song, *Opt. Express*, 2015, **23**, 4435.

26 L. He, J. Ye, M. Shuai, Z. Zhu, X. Zhou, Y. Wang, Y. Li, Z. Su, H. Zhang, Y. Chen, Z. Liu, Z. Cheng and J. Bao, *Nanoscale*, 2015, **7**, 1616–1622.

27 F. Lin, X. Tong, Y. Wang, J. Bao and Z. M. Wang, *Nanoscale Res. Lett.*, 2015, **10**, 435.

28 X. Li, C. W. Magnuson, A. Venugopal, J. An, J. W. Suk, B. Han, M. Borysiak, W. Cai, A. Velamakanni, Y. Zhu, L. Fu, E. M. Vogel, E. Voelkl, L. Colombo and R. S. Ruoff, *Nano Lett.*, 2010, **10**, 4328–4334.

29 A. Reina, X. Jia, J. Ho, D. Nezich, H. Son, V. Bulovic, M. S. Dresselhaus and J. Kong, *Nano Lett.*, 2009, **9**, 30–35.

30 Z. Sun, Z. Yan, J. Yao, E. Beitler, Y. Zhu and J. M. Tour, *Nature*, 2010, **468**, 549–552.

31 D. Wei, Y. Liu, Y. Wang, H. Zhang, L. Huang and G. Yu, *Nano Lett.*, 2009, **9**, 1752–1758.

32 Y. Hernandez, V. Nicolosi, M. Lotya, F. M. Blighe, Z. Sun, S. De, I. T. McGovern, B. Holland, M. Byrne, Y. K. Gun'Ko, J. J. Boland, P. Niraj, G. Duesberg, S. Krishnamurthy, R. Goodhue, J. Hutchison, V. Scardaci, A. C. Ferrari and J. N. Coleman, *Nat. Nanotechnol.*, 2008, **3**, 563–568.

33 M. Lotya, P. J. King, U. Khan, S. De and J. N. Coleman, *ACS Nano*, 2010, **4**, 3155–62.

34 A. O'Neill, U. Khan, P. N. Nirmalraj, J. Boland and J. N. Coleman, *J. Phys. Chem. C*, 2011, **115**, 5422–5428.

35 I. Ogino, Y. Yokoyama, S. Iwamura and S. R. Mukai, *Chem. Mater.*, 2014, **26**, 3334–3339.

36 J. I. Paredes, S. Villar-Rodil, A. Martínez-Alonso and J. M. D. Tascón, *Langmuir*, 2008, **24**, 10560–10564.

37 X. Qi, T. Zhou, S. Deng, G. Zong, X. Yao and Q. Fu, *J. Mater. Sci.*, 2014, **49**, 1785–1793.

38 L. Zhang, J. Liang, Y. Huang, Y. Ma, Y. Wang and Y. Chen, *Carbon N. Y.*, 2009, 47, 3365–3368.

39 L. Peng, Z. Xu, Z. Liu, Y. Wei, H. Sun, Z. Li, X. Zhao and C. Gao, *Nat. Commun.*, 2015, **6**, 5716.

40 D. W. Kim, D. Kim, B. H. Min, H. Lee and H.-T. Jung, *Carbon N. Y.*, 2015, **88**, 126–132.

41 X. Sun, D. Luo, J. Liu and D. G. Evans, *ACS Nano*, 2010, **4**, 3381–3389.

42 T.-Z. Shen, S.-H. Hong and J.-K. Song, *Carbon N. Y.*, 2014, **80**, 560–564.

43 W. Zhang, X. Zou, H. Li, J. Hou, J. Zhao, J. Lan, B. Feng and S. Liu, *RSC Adv.*, 2015, **5**, 146–152.

44 X. Wang, H. Bai and G. Shi, *J. Am. Chem. Soc.*, 2011, **133**, 6338–6342.

45 V. Nicolosi, M. Chhowalla, M. G. Kanatzidis, M. S. Strano and J. N. Coleman, *Science (80-.).*, 2013, **340**, 1226419–1226419.

46 O. Yu Posudievsky, O. A. Khazieieva, A. S. Kondratyuk, V. V Cherepanov, G. I. Dovbeshko, V. G. Koshechko and V. D. Pokhodenko, .

47 J. N. Coleman, M. Lotya, A. O'Neill, S. D. Bergin, P. J. King, U. Khan, K. Young, A. Gaucher, S. De, R. J. Smith, I. V Shvets, S. K. Arora, G. Stanton, H.-Y. Kim, K. Lee, G. T. Kim, G. S. Duesberg, T. Hallam, J. J. Boland, J. J. Wang, J. F. Donegan, J. C. Grunlan, G. Moriarty, A. Shmeliov, R. J. Nicholls, J. M. Perkins, E. M. Grieveson, K. Theuwissen, D. W. McComb, P. D. Nellist and V. Nicolosi, *Science (80-.).*, 2011, **331**, 568–71.

48 L.-S. Lin, W. Bin-Tay, Z. Aslam, A. V. K. Westwood and R. Brydson, *J. Phys. Conf. Ser.*, 2017, **902**, 012026.

49 D.-W. Shin, M. D. Barnes, K. Walsh, D. Dimov, P. Tian, A. I. S. Neves, C. D. Wright, S. M. Yu, J.-B. Yoo, S. Russo and M. F. Craciun, *Adv. Mater.*, 2018, **30**, 1802953.

50 M. Osipova, Y. V. Grachev and V. G. Bespalov, in *Asia Communications and Photonics Conference 2014*, OSA, Washington, D.C., 2014, p. AF4A.5.